

All-Altermagnetic Tunnel Junction of RuO₂/NiF₂/RuO₂

Long Zhang¹, Guangxin Ni^{2,3}, Xuehao Wu⁴, Guoying Gao^{1,*}

¹School of Physics and Wuhan National High Magnetic Field Center, Huazhong University of Science and Technology, Wuhan 430074, People's Republic of China

²Department of Physics, Florida State University, Tallahassee, Florida 32306, USA

³National High Magnetic Field Laboratory, Tallahassee, Florida 32310, USA

⁴Department of Physics, Columbia University, New York, NY 10027, USA

*Email: guoying_gao@mail.hust.edu.cn

ABSTRACT: Emerging altermagnets offer a promising avenue for spintronics, yet their integration into magnetic tunnel junctions has been hindered by reliance on ferromagnetic electrodes (introducing stray fields) or by limited functionality (non-tunable magnetoresistance without spin filtering). Here, we propose an all-altermagnetic tunnel junction (AAMTJ) paradigm composed exclusively of altermagnets — exemplified by experimentally feasible RuO₂/NiF₂/RuO₂. Giant tunneling magnetoresistances of 11,704%, 2,496% and 1,892%, and high spin-filtering of ~90% are achieved. This architecture unlocks tunable multistate magnetoresistance and spin filtering via magnetization control of the electrodes and barrier, stemming from their synergistic and antagonistic alignments of momentum-dependent altermagnetic spin-splitting. Our AAMTJ inherently exhibits low consumption and zero stray field, with nonrelativistic spin splitting and vanishing magnetic moment, combining the advantages of both ferromagnetic and antiferromagnetic tunnel junctions. This AAMTJ paradigm provides a practically versatile platform to realize the revolutionarily potential of altermagnets for reconfigurable magnetic memory devices.

KEYWORDS: *altermagnet, magnetic tunnel junction, magnetoresistance, spin filtering, RuO₂*

Altermagnets¹ represent an emerging class of collinear magnetic systems characterized by a vanishing net magnetic moment and momentum-dependent nonrelativistic spin splitting with *d*-, *g*-, or *i*-wave spin-momentum interactions. Altermagnetism arises from specific spin and crystal

symmetries with time-reversal-breaking magneto-responses.^{2,3} Several altermagnetic (AM) materials include NiF₂,⁴ MnTe,⁵ CrSb,⁶ and KV₂Se₂O,⁷ have been experimentally realized. Spin-splitting switching in RuO₂,⁸ CrSb,⁶ and Mn₅Si₃⁹ has been demonstrated experimentally, confirming their potential for controlling spin-polarized currents. By transcending the conventional dichotomy of antiferromagnets and ferromagnets,¹⁰⁻¹² altermagnets, possessing immunity to stray-field interference, fast spin dynamics, high nonvolatility, and low consumption,^{13,14} hold significant promise for applications in magnetic memory and logic devices.^{15,16}

In magnetic random-access memory, conventional magnetic tunnel junctions (MTJs) typically comprise two ferromagnetic (FM) electrodes with high spin polarization, separated by a non-magnetic semiconducting or insulating barrier.^{17,18} Their operation relies on tunneling magnetoresistance (TMR) and spin-filtering effects arising from the relative magnetization alignment of the electrodes. Altermagnets have been incorporated into MTJs in three primary configurations: (1) An AM metal serving as one electrode, paired with a FM half-metal (HM) or near-HM electrode (e.g., RuO₂/TiO₂/CrO₂¹⁹ and CrSb/In₂Se₃/Fe₂GaTe₂²⁰); (2) An AM semiconductor or insulator acting as the barrier layer, combined with a FM HM electrode (e.g., IrO₂/MnF₂/CrO₂²¹); (3) Two AM layers separated by a non-magnetic barrier (e.g., RuO₂/TiO₂/RuO₂²² and Ag/V₂Te₂O/BiOCl/V₂Te₂O/Ag²³), where TMR stems from the relative orientation of AM spin splitting. However, these designs face critical limitations. In configurations (1) and (2), device performance depends heavily on the FM electrodes rather than the altermagnets themselves, and these junctions inherently produce stray magnetic fields. Configuration (3) offers limited resistance states, features a single non-tunable TMR, and lacks spin-filtering capability. These constraints significantly hinder the practical implementation of AM-based tunnel junctions, underscoring the need for improved designs.

To overcome these challenges, we propose an all-altermagnetic tunnel junction (AAMTJ), schematically illustrated in Figure 1(a), where both electrodes and the barrier layer consist entirely of AM materials. This design eliminates dependence on FM HMs, thereby removing stray fields and enabling fast spin dynamics. The AM magnetization orientations of the two AM electrodes and the barrier provide multiple controllable degrees of freedom. Switching the AM spin-splitting is anticipated to generate substantial TMR and spin-filtering effects, offering high nonvolatility

and low power consumption. Experimentally realized altermagnets, RuO₂²⁴ (metal) and NiF₂⁴ (insulator), are selected to construct the AAMTJ, serving as electrodes and barrier, respectively. Both RuO₂ and NiF₂ share a rutile structure with excellent lattice matching, facilitating high-quality heterostructures fabrication.

In this Letter, we investigate a RuO₂/NiF₂/RuO₂ AAMTJ using the nonequilibrium Green's function (NEGF) approach combined with density functional theory (DFT). By controlling the magnetization alignments of the electrode and barrier, the AM spin splitting can be flipped, producing multiple distinct tunneling states. This AAMTJ exhibits widely tunable TMRs ranging from 30% to 11,704%, and high and low spin-filtering efficiencies, establishing it as a compelling platform for exploring multi-controlled AM spin transport with zero stray field, high nonvolatility, and low energy consumption.

First-principles calculations are performed using DFT within the Vienna ab initio Simulation Package (VASP).²⁵ The Perdew-Burke-Ernzerhof (PBE) exchange-correlation functional of the generalized gradient approximation (GGA)²⁶ is employed, incorporating a Hubbard U .²⁷ According to earlier studies, the U_{eff} is set to 4 eV for Ni-3d orbitals²⁸ and 2 eV for Ru-4d orbitals.^{29,30} A plane-wave cutoff energy of 600 eV is utilized, with convergence criteria of 10⁻⁶ eV for energy and 0.001 eV/Å for force. Monkhorst-Pack k -meshes of $7 \times 7 \times 14$ and $10 \times 10 \times 14$ are utilized for (110) and (001) faces, respectively. Using DFT combined with the NEGF approach, spin transport properties are calculated in the QuantumWise Atomistix Toolkit (ATK) package.³¹ A cutoff energy of 150 Hartree and k -meshes $14 \times 7 \times 150$ and 150×150 are used for self-consistent and transmission calculations, respectively. All materials and AAMTJs are fully relaxed. Similar computational methods have been applied in our previous works.^{20,32,33}

The rutile-type NiF₂ and RuO₂ structures exhibit centro-symmetry, with magnetic Ni and Ru atoms serving as their inversion centers, respectively. Both NiF₂ and RuO₂ crystallize in the $P4_2/mnm$ space group, and their crystal structures for the (110) and (001) surfaces are displayed in Figure 2(a,b). The spin-resolved charge densities [Figure 2(c,d)] demonstrate their AM configurations, with two opposite magnetic sublattices, The Ni atoms in NiF₂ and the Ru atoms in RuO₂ exhibit atomic magnetic moments of ± 1.78 and $\pm 1.16 \mu_B$, respectively. Their magnetic space group is $P4'_2/mnm'$, violating the $TP\tau$ and $U\tau$ symmetries, where T , P , τ , and U stand for the time reversal, spatial inversion, half lattice translation, and spinor symmetry, respectively. Both

materials display d -wave symmetry, with their opposite magnetic sublattices related by a 90° planar rotation (C_{4z}).

The high-symmetry points within the Brillouin zone are illustrated in Figure 2(e). As shown in Figure 2(f-i), NiF₂ and RuO₂ possess insulating (band gap of 4.29 eV) and metallic features, respectively. Our calculated spin-resolved electronic structures [Figure 2(f-i)] are consistent with previous reports.^{19,28} The broken PT symmetries of NiF₂ and RuO₂ allow for momentum-dependent and nonrelativistic spin splitting, forming symmetry-connected spin-momentum locking. This effect arises from exchange coupling rather than spin-orbit coupling (SOC). Pronounced spin splitting appears along the Γ -X path for the (110) face and along the M- Γ path for the (001) face, suggesting that the [110] transport direction can yield spin polarization. In contrast, the spin-resolved bands remain degenerate along the Γ -Z path, indicating the absence of spin discrimination for transport along the [001] direction. This orientation-dependent nature of AM spin transport has been verified previously.^{19,21} Thus, the [110] transport direction is the focus herein. The orbital behaviors of the dominant atoms near the Fermi level further explicate the electronic and spin properties. Along the Γ -X path, the valence band maximum (VBM) of NiF₂ arises mainly from spin-up Ni- d_{yz} and spin-down Ni- d_{xz} orbitals, while the conduction band minimum (CBM) is dominated by Ni- $d_{x^2-y^2}$ and Ni- d_{z^2} orbitals in both spin channels [Figure S1(a)]. Similarly, the spin splitting near the Fermi level in RuO₂ is primarily governed by spin-up Ru- d_{xz} and spin-down Ru- d_{yz} orbitals [Figure S1(b)].

Considering the structural, electronic, and magnetic properties of NiF₂ and RuO₂, together with their experimental confirmed altermagnetism,^{4,24} the RuO₂/NiF₂/RuO₂ AAMTJ is constructed along the [110] direction [Figure 3(a)]. Rutile NiF₂/RuO₂ with (110) face possesses lattice constants of $a = b = 4.65/4.55 \times \sqrt{2} = 6.58/6.43 \text{ \AA}$ and $c = 3.08/3.14 \text{ \AA}$, consistent with reported values.^{28,34} The lattice mismatch is calculated as $\Delta = (a_1 - a_2)/a_2 \times 100\%$, in which a_1 and a_2 stand for the lattice constants of the two materials. The resulting lattice mismatch of c and a in our AAMTJ is only 1.7% and 2.2%, respectively, which is smaller than the experimentally demonstrated 6.5% in Fe/MgAlO_x/Fe₄N³⁵ and 4.3% in Co₂MnSi/MgO/Co₂MnSi,³⁶ confirming its structural feasibility. Two possible magnetization orientations are considered for both the NiF₂

barrier (M_{2-1}/M_{2-2}) and the right RuO_2 (M_{3-1}/M_{3-2}) electrode [Figure 3(a)]. Consequently, four distinct magnetization configurations (S1-S4) are examined in this AAMTJ [Figure 3(b)].

A high TMR ratio indicates a pronounced resistance contrast between data bits (“0” and “1”), while perfect (100%) spin-filtering efficiency transmits electrons selectively and efficiently, improving TMR and data fidelity. Both characteristics are crucial for high-performance and nonvolatile magnetic memory devices. The TMR is defined as $\text{TMR} = (T_{\text{P}} - T_{\text{AP}}) / T_{\text{AP}} \times 100\%$, where $T_{\text{P}} = \sum_{\vec{k}_{//}} T_{\text{P}}(\vec{k}_{//}) / N_k$ and $T_{\text{AP}} = \sum_{\vec{k}_{//}} T_{\text{AP}}(\vec{k}_{//}) / N_k$ denote the transmission coefficients for parallel (P) and antiparallel (AP) magnetization alignments, respectively. The in-plane wave vector $\vec{k}_{//} = (k_x, k_y)$ is perpendicular to the transport direction. The spin-filtering efficiency η is attained from $\eta = (T_{\uparrow} - T_{\downarrow}) / (T_{\uparrow} + T_{\downarrow}) \times 100\%$, with T_{\uparrow} and T_{\downarrow} are the transmission coefficients for the spin-up and spin-down channels, respectively. The spin- and $\vec{k}_{//}$ -transmission spectra of the $\text{RuO}_2/\text{NiF}_2/\text{RuO}_2$ AAMTJ in energy and momentum space [Figure 3(c-l)] are schematically illustrated in Figure 1(b). The calculated values of T_{\uparrow} , T_{\downarrow} , η , and TMR are listed in Table 1 and 2, which include six combinations of P and AP magnetization alignments.

For the state S1, the spin-up transmission is predominantly localized along the Γ -Y line [Figure 3(e)], while the spin-down transmission is distributed between the Γ -X and Y-M paths [Figure 3(f)]. The dominance of spin-up channel results in a high η of 93%. In contrast, in state S2, the transmission for both channels is concentrated near the Γ point and along the Γ -Y line [Figure 3(g,h)], yielding comparable transmission coefficients and a low η of -19%. Similarly, pronounced transmission along the Γ -Y line is observed for the spin-up (spin-down) channel in state S3 (S4), resulting in high η value of 85% (-90%). A positive (negative) η indicates preferential tunneling of spin-up (spin-down) electrons. The ability to selectively filter different spin channels under distinct magnetization states highlights the tunability and versatility of spin transport in the AAMTJ, which is advantageous for practical spintronic applications.

These transport phenomena can be further understood from the spin-resolved band structures along the [110] transport direction. NiF_2 exhibits dominant spin-up character at both the VBM and CBM along the Γ -X path [Figure 2(f)]. Similarly, RuO_2 shows predominant spin-up bands near the Fermi level along this direction [Figure 2(g)]. This spin character facilitates efficient spin-up electron tunneling, leading to the large T_{\uparrow} observed in state S1. For the state S2, the magnetization

reversal of the right RuO₂ electrode shifts its dominant near-Fermi-level bands to the spin-down channel, producing a strong mismatch with the spin-up-favored left electrode and barrier. This misalignment severely suppresses tunneling in both spin channels, leading to a giant TMR of 11,704% between state S1(P) vs state S2(AP) (considering states S1 and S2 as the P and AP alignments, respectively). This value surpasses most reported altermagnet-based junctions, such as 1,056% of CrSb/In₂Se₃/Fe₂GaTe₂,²⁰ 574% of Ag/Ve₂Te₂O/BiOCl/V₂Te₂O/Ag,²³ and 6,100% of RuO₂/TiO₂/CrO₂.¹⁹ Such an exceptionally giant TMR reflects the large difference between the high- and low-resistance states, thereby reducing read/write error rates and improving device reliability. Even under equilibrium conditions ($E=0$) with the same magnetization reversal of the right RuO₂ electrode, the 11,704% TMR of our AAMTJ far exceeds the 200% TMR previously reported in RuO₂/TiO₂/RuO₂.²² This enhancement originates from the altermagnetic NiF₂ barrier, which selectively promotes spin-up tunneling and suppresses spin-down tunneling owing to spin-differential contribution along the transport Γ -X direction [Figure 2(f)]. Consequently, the AM NiF₂ barrier amplifies the transport contrast between the P and AP states in RuO₂/NiF₂/RuO₂, in stark contrast to non-magnetic TiO₂ barrier with nearly identical tunneling for both spin channels in RuO₂/TiO₂/RuO₂.

State S3 differs from state S1 by a magnetization reversal of the NiF₂ barrier, which moderately suppresses transmission in both spin channels. Nevertheless, since both RuO₂ electrodes continue to favor spin-up transport, T_{\uparrow} in state S3 remains larger than T_{\downarrow} . The combination between state S1(P) and state S3(AP) yields a large TMR of 2,496%, which exceeds the 150-170% reported for NiF₂-based junctions employing non-magnetic electrodes and barriers.²⁸ This result highlights the superiority of AM electrodes in our AAMTJ, which provide strong spin-polarized currents owing to the spin-up dominated bands near the Fermi level along [110] direction in RuO₂ [Figure 2(g)].

Notably, the spin-splitting flip in the conductive RuO₂ electrodes exerts a more pronounced impact on transmission than that of the wide-gap NiF₂ barrier. While NiF₂ primarily mediates tunneling, the RuO₂ electrodes directly determine the available conducting states at the Fermi level. Consequently, the total transmission in state S3 is higher than in state S2, leading to a TMR of 355% for state S3(P) vs state S2(AP). This finding demonstrates that, in an AAMTJ, spin

switching within the AM electrodes has a stronger effect on transport modulation than magnetization reversal within the AM barrier.

In state S4, the magnetizations of both the NiF₂ barrier and the right RuO₂ electrode are flipped relative to state S1. The resulting spin-splitting mismatch reduces the overall transmission, yielding a TMR of 1,892% between state S1 (P) and S4 (AP). Tunneling is more efficient when the barrier and the right electrode share the same dominant spin channel (spin-down in state S4) than when they are opposite, as in state S2. This alignment leads to a higher total transmission in state S4 than in state S2, producing a TMR of 493% between state S4 (P) and S2 (AP). Additionally, for state S4(P) vs state S3(AP), the spin-splitting of the NiF₂ barrier is mismatched with the left RuO₂ electrode, strongly suppressing tunneling regardless of the right electrode's alignments, yielding a low TMR of 30%. The large variation in TMR from 11,704% to 30% achieved by flipping the magnetizations of the electrode and barrier highlights the AAMTJ's multistate functionality and its potential for practical controllability.

The spin-resolved local density of states (LDOS) [Figure 4(a-h)] and spin- and layer-resolved projected device density of states (PDDOS) [Figure 5(a-d)] further corroborate these interpretations derived from the spin-resolved band structures and transport calculations. The left RuO₂ electrode is taken as the source. For state S1 (Figures 4(a,b) and 5(a)), the predominance of spin-up electron tunneling is confirmed by a pronounced spin-up PDDOS peak near the Fermi level within the right electrode region, exceeding the spin-down counterpart. This clearly demonstrates efficient spin-down filtering. The overall density of states (DOS) in state S1 is higher than those in states S2, S3, and S4, validating the origin of the high TMR when state S1 serves as the P configuration. In contrast, state S2 exhibits substantially diminished electronic states for both spin channels near the Fermi level [Figures 4(c,d) and 5(b)] due to mismatched transport channels between the electrodes, consistent with its poor spin-filtering efficiency. Conversely, states S3 and S4 display a distinct predominance of spin-up and spin-down states [Figures 4(e,h) and 5(c,d)], respectively, with majority-spin densities not only exceeding the opposite spin channel but also surpassing those in either spin channel of state S2. This observation directly accounts for the highly spin-polarized tunneling in states S3 and S4, and the moderate TMRs achieved when these states are configured as P against state S2 as AP.

To conclude, we have proposed an AAMTJ architecture composed exclusively of AM systems [Figure 1(a)], exemplified by RuO₂ electrodes and a NiF₂ barrier. With zero net magnetic moment and nonrelativistic spin splitting across the entire device, the AAMTJ combines the advantages of ferromagnets (spin polarization and high controllability) and antiferromagnets (zero stray field and fast spin dynamics), while avoiding their respective drawbacks. The AAMTJ architecture unlocks multistate spin transport, accompanied by widely tunable TMR and spin filtering achieved by flipping the AM spin splitting through controlled magnetization of the electrodes and barrier [Figure 1(b)]. Within this fully AM platform, giant tunneling TMRs of 11,704%, 2,496% and 1,892%, and high spin-filtering efficiency of ~90% are realized. These effects arise from the synergistic and antagonistic spin-splitting alignments between the AM electrodes and barrier. Our AAMTJ pioneers a versatile platform for fully exploiting altermagnetism in next-generation spintronic devices and will stimulate subsequent theoretical and experimental explorations into AM tunnel junctions.

ASSOCIATED CONTENT

AUTHOR INFORMATION

Corresponding Author

Guoying Gao – School of Physics and Wuhan National High Magnetic Field Center, Huazhong University of Science and Technology, Wuhan 430074, People’s Republic of China; <https://orcid.org/0000-0002-0606-3593>; Email: guoying_gao@mail.hust.edu.cn

Authors

Long Zhang – School of Physics and Wuhan National High Magnetic Field Center, Huazhong University of Science and Technology, Wuhan 430074, People’s Republic of China; <https://orcid.org/0009-0003-6193-1642>

Guangxin Ni – Department of Physics, Florida State University, Tallahassee, Florida 32306, USA; National High Magnetic Field Laboratory, Tallahassee, Florida 32310, USA; <https://orcid.org/0000-0002-7216-1829>

Xuehao Wu – Department of Physics, Columbia University, New York, NY 10027, USA

Notes

The authors declare no competing financial interest.

ACKNOWLEDGMENTS

Guoying Gao acknowledges support from the National Natural Science Foundation of China (Grant No. 12174127). Guangxin Ni acknowledges support from the U.S. Department of Energy (DE-SC0022022), the U.S. National Science Foundation (DMR-2145074), and the ACS Petroleum Research Grant (PRF# 66465-DNI10).

REFERENCES

- (1) Šmejkal, L.; Sinova, J.; Jungwirth, T. Beyond Conventional Ferromagnetism and Antiferromagnetism: A Phase with Nonrelativistic Spin and Crystal Rotation Symmetry. *Phys. Rev. X* **2022**, *12*, 031042.
- (2) Liu, Z.; Medhekar, N. V. *d*-Wave Polarization-Spin Locking in Two-Dimensional Altermagnets. *Nano Lett.* **2025**, *25*, 13411-13418.
- (3) Sun, W.; Wang, W.; Yang, C.; Hu, R.; Yan, S.; Huang, S.; Cheng, Z. Altermagnetism Induced by Sliding Ferroelectricity via Lattice Symmetry-Mediated Magnetoelectric Coupling. *Nano Lett.* **2024**, *24*, 11179-11186.
- (4) Hariki, A.; Sakurai, K.; Okauchi, T.; Kuneš, J. Separating altermagnetic and ferromagnetic effects in X-ray magnetic dichroism of rutile NiF₂. *npj Quantum Mater.* **2025**, *10*, 49.
- (5) Osumi, T.; Souma, S.; Aoyama, T.; Yamauchi, K.; Honma, A.; Nakayama, K.; Takahashi, T.; Ohgushi, K.; Sato, T. Observation of a giant band splitting in altermagnetic MnTe. *Phys. Rev. B* **2024**, *109*, 115102.
- (6) Zhou, Z.; Cheng, X.; Hu, M.; Chu, R.; Bai, H.; Han, L.; Liu, J.; Pan, F.; Song, C. Manipulation of the altermagnetic order in CrSb via crystal symmetry. *Nature* **2025**, *638*, 645-650.
- (7) Jiang, B.; Hu, M.; Bai, J.; Song, Z.; Mu, C.; Qu, G.; Li, W.; Zhu, W.; Pi, H.; Wei, Z.; Sun, Y.-J.; Huang, Y.; Zheng, X.; Peng, Y.; He, L.; Li, S.; Luo, J.; Li, Z.; Chen, G.; Li, H.; Weng, H.; Qian, T. A metallic room-temperature *d*-wave altermagnet. *Nat. Phys.* **2025**, *21*, 754-759.
- (8) Xu, S.; Zhang, Z.; Mahfouzi, F.; Huang, Y.; Cheng, H.; Dai, B.; Kim, J.; Zhu, D.; Cai, W.; Shi, K.; Guo, Z.; Cao, K.; Hong, B.; Liu, Y.; Yang, J.; Zhang, K.; Cao, J.; Zhu, F.; Tai, L.; Wang, Y.; Eimer, S.; Fert, A.; Wang, K. L.; Kioussis, N.; Zhang, Y.; Zhao, W. Giant Spin-flop magnetoresistance in a collinear antiferromagnetic tunnel junction. *Nat. Commun.* **2025**, *16*, 8370.
- (9) Han, L.; Fu, X.; Peng, R.; Cheng, X.; Dai, J.; Liu, L.; Li, Y.; Zhang, Y.; Zhu, W.; Bai, H.; Zhou, Y.; Liang, S.; Chen, C.; Wang, Q.; Chen, X.; Yang, L.; Zhang, Y.; Song, C.; Liu, J.; Pan, F. Electrical 180° switching of Néel vector in spin-splitting antiferromagnet. *Sci. Adv.* **2024**, *10*, eadn0479.

- (10) Liu, Y.; Zhang, L.; Wu, X.; Gao, G. Magnetic phase transition, enhanced magnetic anisotropy, and anomalous Hall effect in bilayer FeCl₂ with different stacking orders. *Appl. Phys. Lett.* **2025**, *126*, 162404.
- (11) Bai, L.; Feng, W.; Liu, S.; Šmejkal, L.; Mokrousov, Y.; Yao, Y. Altermagnetism: Exploring New Frontiers in Magnetism and Spintronics. *Adv. Funct. Mater.* **2024**, *34*, 2409327.
- (12) Zhang, L.; Liu, Y.; Wu, M.; Gao, G. Electric-Field- and Stacking-Tuned Antiferromagnetic FeClF Bilayer: The Coexistence of Bipolar Magnetic Semiconductor and Anomalous Valley Hall Effect. *Adv. Funct. Mater.* **2025**, *35*, 2417857.
- (13) Wu, Y.; Deng, L.; Yin, X.; Tong, J.; Tian, F.; Zhang, X. Valley-Related Multipiezo Effect and Noncollinear Spin Current in an Altermagnet Fe₂Se₂O Monolayer. *Nano Lett.* **2024**, *24*, 10534-10539.
- (14) Zhu, Y.; Chen, T.; Li, Y.; Qiao, L.; Ma, X.; Liu, C.; Hu, T.; Gao, H.; Ren, W. Multipiezo Effect in Altermagnetic V₂SeTeO Monolayer. *Nano Lett.* **2024**, *24*, 472-478.
- (15) Liu, C.; Li, X.; Li, X.; Yang, J. Realizing Abundant Two-Dimensional Altermagnets with Anisotropic Spin Current Via Spatial Inversion Symmetry Breaking. *Nano Lett.* **2025**, *25*, 9197-9203.
- (16) Wang, D.; Wang, H.; Liu, L.; Zhang, J.; Zhang, H. Electric-Field-Induced Switchable Two-Dimensional Altermagnets. *Nano Lett.* **2025**, *25*, 498-503.
- (17) Echtenkamp, W.; Dixit, B.; Yang, Y.; Lyu, D.; Peterson, T.; Jia, Q.; Chen, Y. C.; Wang, J. P. Prospects of Electric Field Control in Perpendicular Magnetic Tunnel Junctions and Emerging 2D Spintronics for Ultralow Energy Memory and Logic Devices. *Adv. Funct. Mater.* **2025**, 2505426.
- (18) Yan, Z.; Zhang, X.; Xiao, J.; Fang, C.; Xu, X. Giant Nonvolatile Multistate Resistance with Fully Magnetically Controlled van der Waals Multiferroic Tunnel Junctions. *Nano Lett.* **2025**, *25*, 8473-8479.
- (19) Chi, B.; Jiang, L.; Zhu, Y.; Yu, G.; Wan, C.; Zhang, J.; Han, X. Crystal-facet-oriented altermagnets for detecting ferromagnetic and antiferromagnetic states by giant tunneling magnetoresistance. *Phys. Rev. Appl.* **2024**, *21*, 034038.
- (20) Zhang, L.; Ni, G.; He, J.; Gao, G. Above room temperature multiferroic tunnel junction with the altermagnetic metal CrSb. *Phys. Rev. B* **2025**, *112*, 064401.
- (21) Liu, F.; Zhang, Z.; Yuan, X.; Liu, Y.; Zhu, S.; Lu, Z.; Xiong, R. Giant tunneling magnetoresistance in insulated altermagnet/ferromagnet junctions induced by spin-dependent tunneling effect. *Phys. Rev. B* **2024**, *110*, 134437.
- (22) Jiang, Y.-Y.; Wang, Z.-A.; Samanta, K.; Zhang, S.-H.; Xiao, R.-C.; Lu, W. J.; Sun, Y. P.; Tsymbal, E. Y.; Shao, D.-F. Prediction of giant tunneling magnetoresistance in RuO₂/TiO₂/RuO₂ (110) antiferromagnetic tunnel junctions. *Phys. Rev. B* **2023**, *108*, 174439.
- (23) Cui, Q.; Zhu, Y.; Yao, X.; Cui, P.; Yang, H. Giant spin-Hall and tunneling magnetoresistance effects based on a two-dimensional nonrelativistic antiferromagnetic metal. *Phys. Rev. B* **2023**, *108*, 024410.
- (24) Fedchenko, O.; Minár, J.; Akashdeep, A.; D'Souza, S. W.; Vasilyev, D.; Tkach, O.; Odenbreit, L.; Nguyen, Q.; Kutnyakhov, D.; Wind, N.; Wenthaus, L.; Scholz, M.; Rossnagel, K.; Hoesch, M.; Aeschlimann, M.; Stadtmüller, B.; Kläui, M.; Schönhense, G.; Jungwirth, T.; Hellenes, A. B.; Jakob, G.; Šmejkal, L.; Sinova, J.; Elmers, H.-J. Observation of time-reversal symmetry breaking in the band structure of altermagnetic RuO₂. *Sci. Adv.* **2024**, *10*, eadj4883.

- (25) Kresse, G.; Furthmüller, J. Efficient iterative schemes for ab initio total-energy calculations using a plane-wave basis set. *Phys. Rev. B* **1996**, *54*, 11169-11186.
- (26) Perdew, J. P.; Burke, K.; Ernzerhof, M. Generalized Gradient Approximation Made Simple. *Phys. Rev. Lett.* **1996**, *77*, 3865-3868.
- (27) Aryasetiawan, F.; Karlsson, K.; Jepsen, O.; Schönberger, U. Calculations of Hubbard U from first-principles. *Phys. Rev. B* **2006**, *74*, 125106.
- (28) Samanta, K.; Shao, D.-F.; Tsymbal, E. Y. Spin Filtering with Insulating Altermagnets. *Nano Lett.* **2025**, *25*, 3150-3156.
- (29) Huang, Y.; Lai, J.; Zhan, J.; Yu, T.; Chen, R.; Liu, P.; Chen, X.-Q.; Sun, Y. Ab initio study of quantum oscillations in altermagnetic and nonmagnetic phases of RuO₂. *Phys. Rev. B* **2024**, *110*, 144410.
- (30) Samanta, K.; Jiang, Y.-Y.; Paudel, T. R.; Shao, D.-F.; Tsymbal, E. Y. Tunneling magnetoresistance in magnetic tunnel junctions with a single ferromagnetic electrode. *Phys. Rev. B* **2024**, *109*, 174407.
- (31) Taylor, J.; Guo, H.; Wang, J. Ab initio modeling of quantum transport properties of molecular electronic devices. *Phys. Rev. B* **2001**, *63*, 245407.
- (32) Zhang, L.; Liu, Y.; Ren, J.; Ding, G.; Wang, X.; Ni, G.; Gao, G.; Cheng, Z. Lithium and Vanadium Intercalation into Bilayer V₂Se₂O: Ferrimagnetic-Ferroelastic Multiferroics and Anomalous and Spin Transport. *Adv. Sci.* **2025**, e12533.
- (33) Zhang, L.; Liu, Y.; Xu, Z.; Gao, G. Electronic phase transition, perpendicular magnetic anisotropy and high Curie temperature in Janus FeClF. *2D Mater.* **2023**, *10*, 045005.
- (34) Zhu, Y.; Liu, S.; Cui, Q.; Jiang, J.; Yang, H.; Zhou, T.; Liu, B. Tunneling magnetoresistance in altermagnetic tunnel junctions with the half-metal electrode. *Appl. Phys. Lett.* **2025**, *127*, 082401.
- (35) Ma, T.; Zhu, Y.; Dainone, P. A.; Chen, T.; Devaux, X.; Wan, C.; Migot, S.; Lengaigne, G.; Vergnat, M.; Yan, Y.; Han, X.; Lu, Y. Large Sign Reversal of Tunneling Magnetoresistance in an Epitaxial Fe/MgAlO_x/Fe₄N Magnetic Tunnel Junction. *ACS Appl. Electron. Mater.* **2023**, *5*, 5954-5961.
- (36) Liu, H.-x.; Honda, Y.; Taira, T.; Matsuda, K.-i.; Arita, M.; Uemura, T.; Yamamoto, M. Giant tunneling magnetoresistance in epitaxial Co₂MnSi/MgO/Co₂MnSi magnetic tunnel junctions by half-metallicity of Co₂MnSi and coherent tunneling. *Appl. Phys. Lett.* **2012**, *101*, 132418.

Figures and Tables

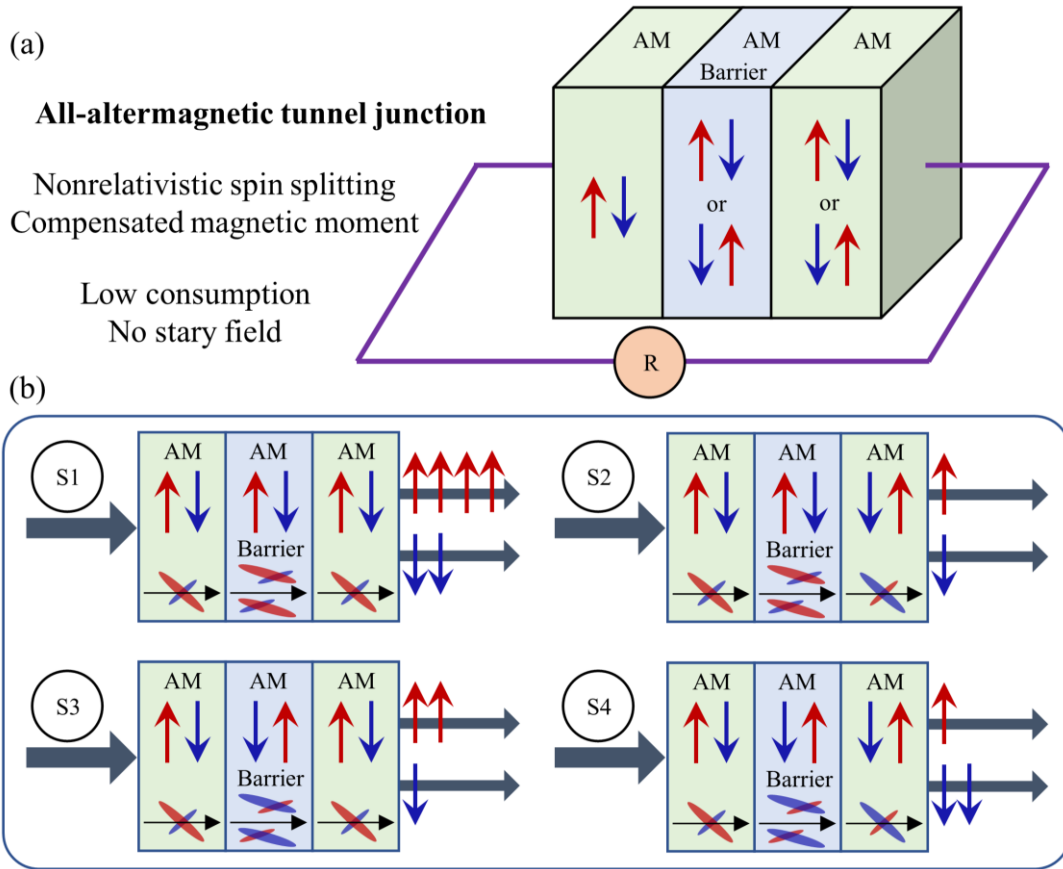


Figure 1. Schematic illustrations of the all-almagnetic tunnel junction (AAMTJ) with varying magnetization configurations (a) and multistate spin transport (b).

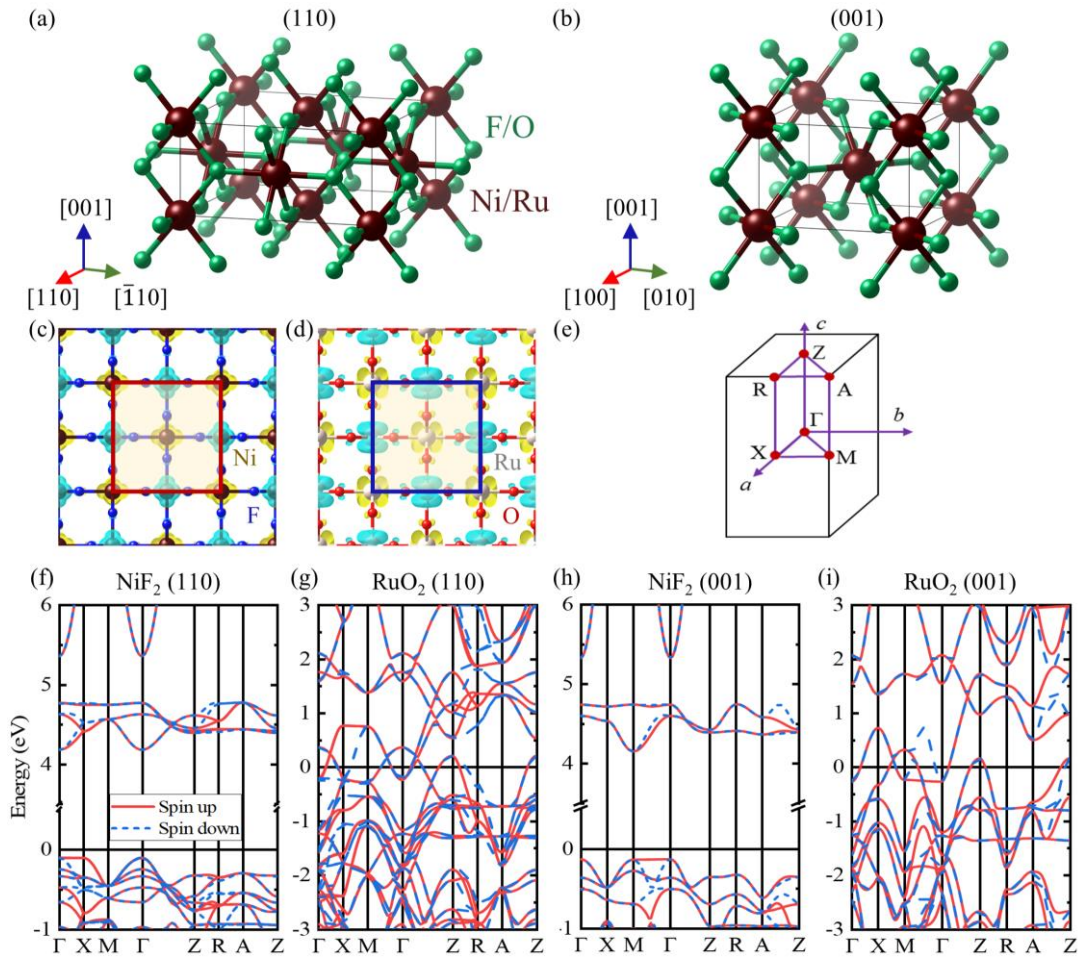


Figure 2. Crystal structures of bulk rutile NiF_2 and RuO_2 with (110) (a) and (001) (b) faces. Spin-resolved charge density with isosurface of 0.01 e/bohr^3 of NiF_2 (c) and RuO_2 (d). Schematic diagram of high-symmetry points within Brillouin zone (e). Spin-resolved band structures of NiF_2 and RuO_2 with (110) (f,g) and (001) (h,i) faces.

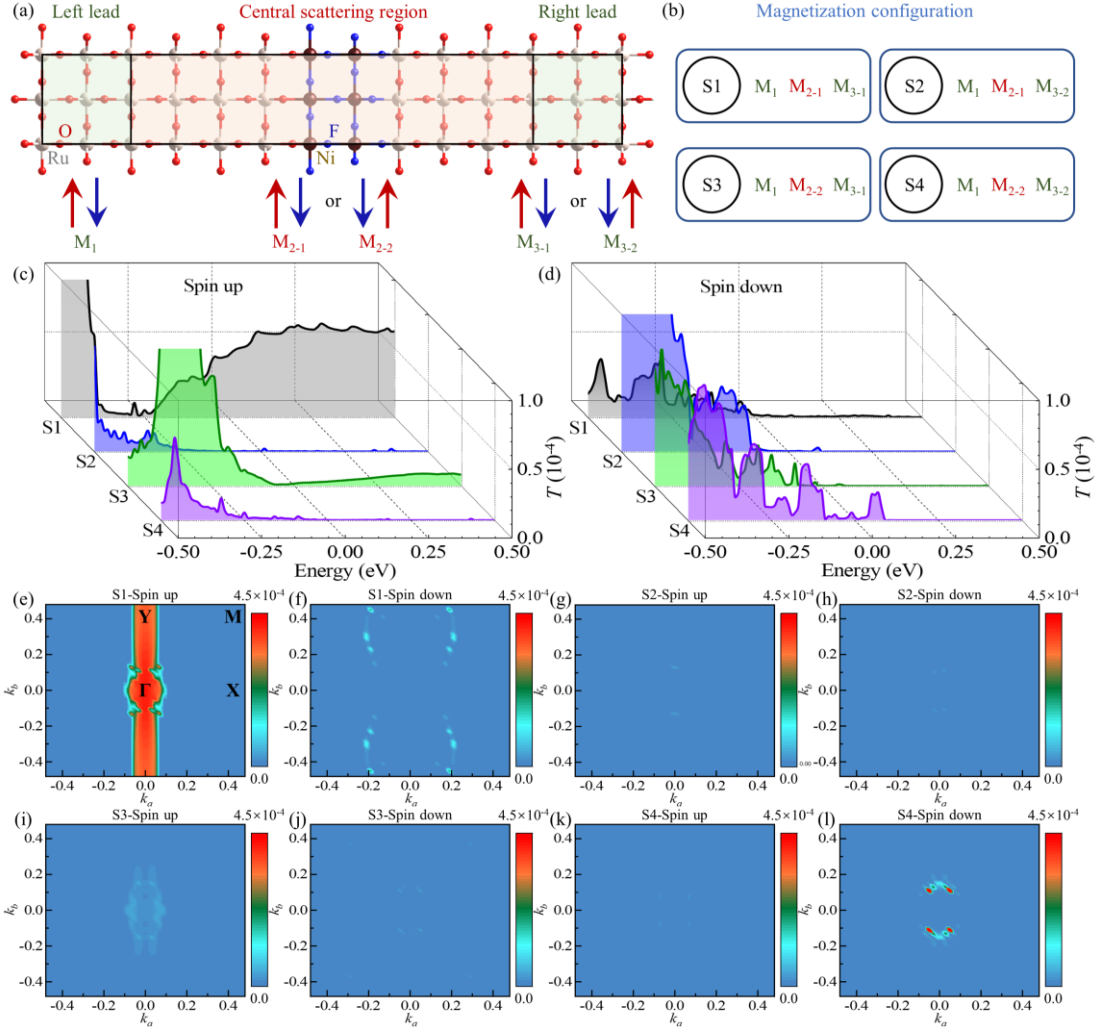


Figure 3. Structural models of the proposed $\text{RuO}_2/\text{NiF}_2/\text{RuO}_2$ AAMTJ (a) and varying magnetization alignments (b). Transmission coefficients as a function of energy in spin-up (c) and spin-down (d) channels. The \vec{k}_{\parallel} -resolved transmission spectra in the 2D Brillouin zone (e-l).

Table 1. Spin-dependent electron transmission T_{\uparrow} and T_{\downarrow} and spin filtering efficiency η across $\text{RuO}_2/\text{NiF}_2/\text{RuO}_2$ AAMTJ in the four magnetic configurations (S1-S4).

	T_{\uparrow}	T_{\downarrow}	T_{tot}	η (%)
S1	4.46×10^{-5}	1.68×10^{-6}	4.62×10^{-5}	93
S2	1.58×10^{-7}	2.34×10^{-7}	3.92×10^{-7}	-19
S3	1.65×10^{-6}	1.30×10^{-7}	1.78×10^{-6}	85
S4	1.11×10^{-7}	2.21×10^{-6}	2.32×10^{-6}	-90

Table 2. Multiple tunneling magnetoresistance (TMR) across $\text{RuO}_2/\text{NiF}_2/\text{RuO}_2$ AAMTJ with varying parallel (P) and antiparallel (AP) alignments.

(P, AP)	TMR (%)
(S1, S2)	11,704
(S1, S3)	2,496
(S1, S4)	1,892
(S3, S2)	355
(S4, S2)	493
(S4, S3)	30

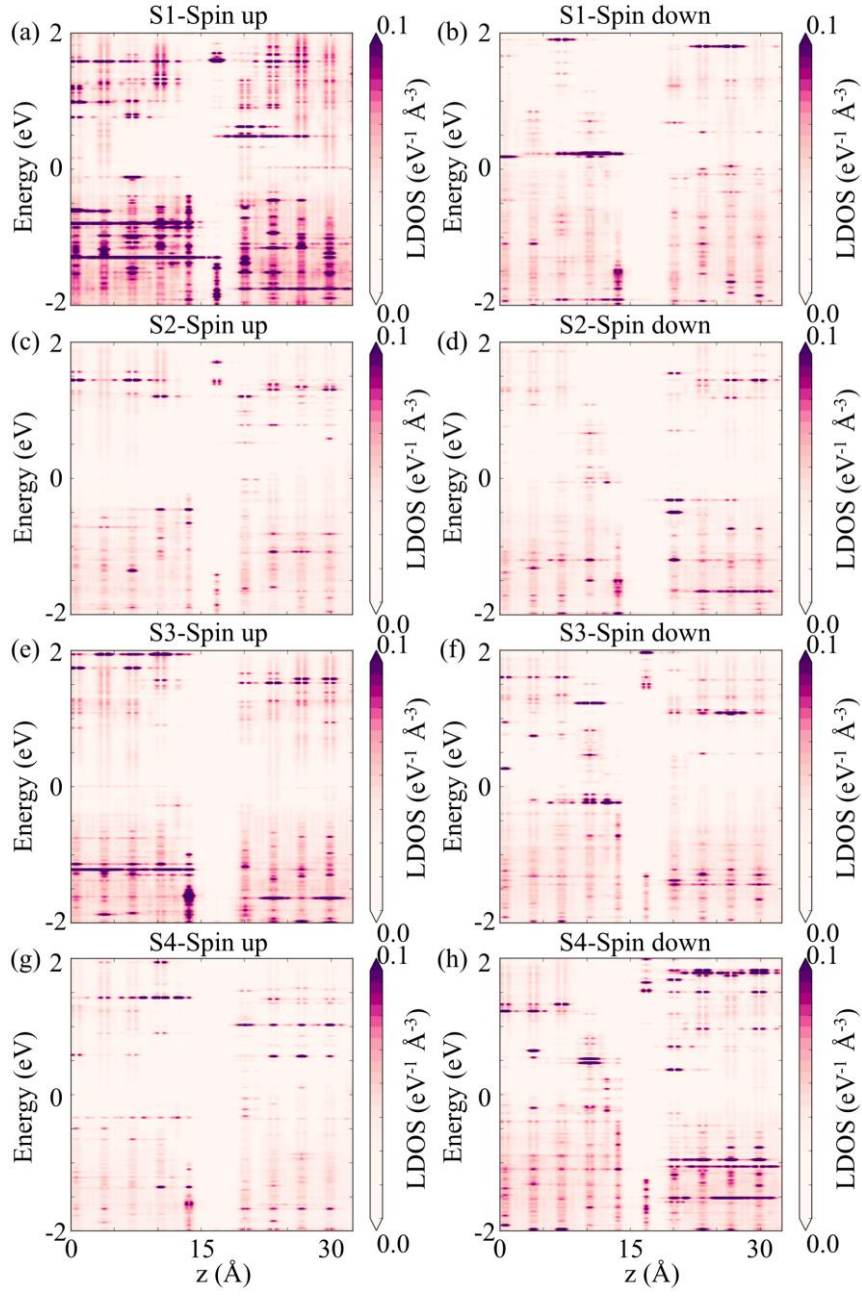


Figure 4. The spin-resolved local density of states (LDOS) across RuO₂/NiF₂/RuO₂ AAMTJ with four magnetic configurations (S1-S4). The source of contribution is set as the left RuO₂ electrode.

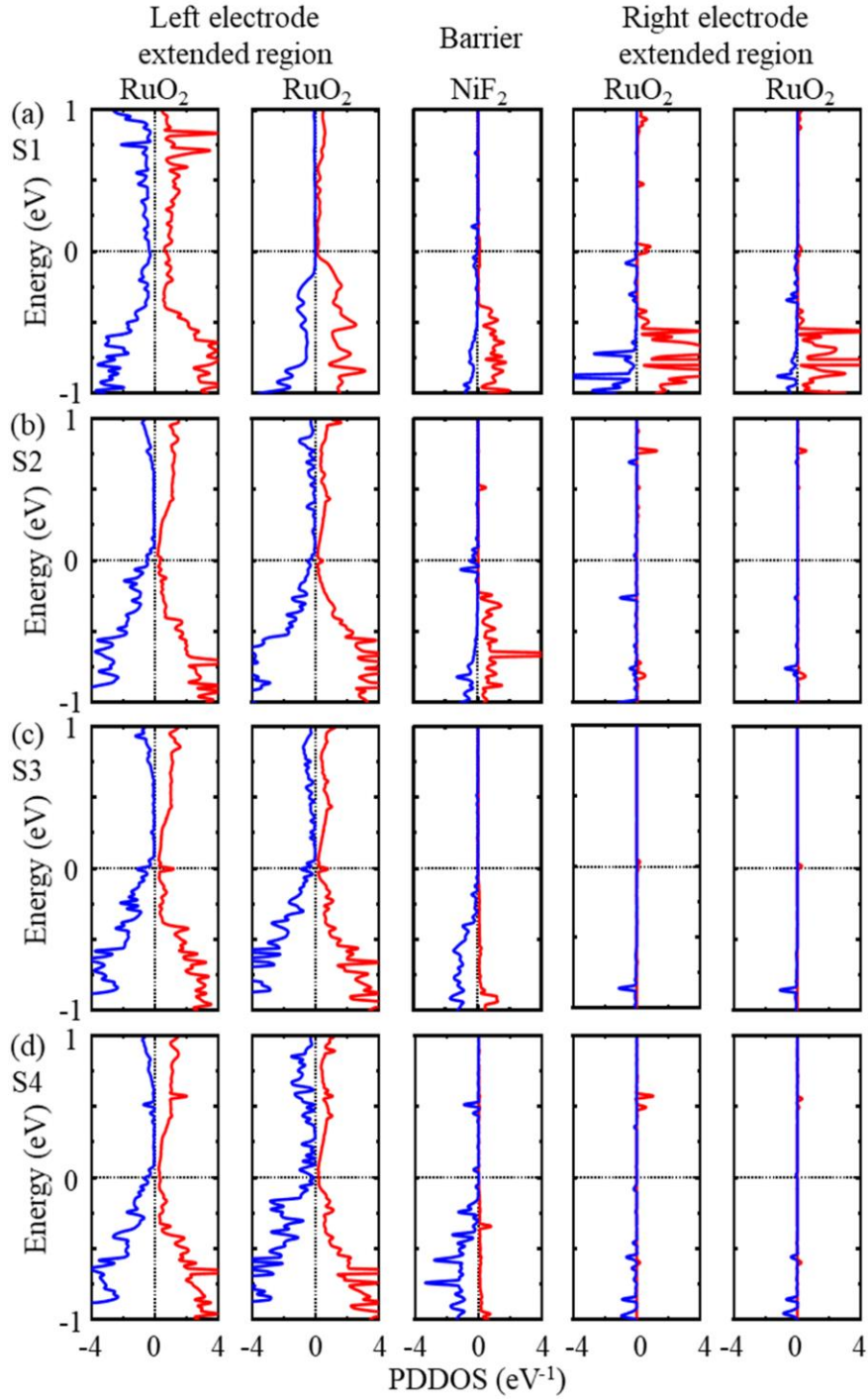


Figure 5. The spin- and layer-resolved projected device density of states (PDDOS) across $\text{RuO}_2/\text{NiF}_2/\text{RuO}_2$ AAMTJ with four magnetic configurations. The source of contribution is set as the left RuO_2 electrode.